Cite as: A. Cugurra *et al*., *Science* 10.1126/science.abf7844 (2021).

Skull and vertebral bone marrow are myeloid cell reservoirs for the meninges and CNS parenchyma

Andrea Cugurra[1,2]†, Tornike Mamuladze[3]†, Justin Rustenhoven[3]†, Taitea Dykstra[3], Giorgi Beroshvili[3], Zev J. Greenberg[4], Wendy Baker[2], Zach Papadopoulos[3,5], Antoine Drieu[3], Susan Blackburn[3], Mitsuhiro Kanamori[3], Simone Brioschi[3], Jasmin Herz[3], Laura G. Schuettpelz[4], Marco Colonna[3], Igor Smirnov[3], Jonathan Kipnis[1,2,3,5]*

[1]Gutenberg Research Fellowship Group of Neuroimmunology, Focus Program Translational Neuroscience (FTN) and Immunotherapy (FZI), Rhine Main Neuroscience Network (rmn[2]), University Medical Center of the Johannes Gutenberg University Mainz, Mainz, Germany. [2]Department of Neuroscience, School of Medicine, University of Virginia, Charlottesville, VA, USA. [3]Department of Pathology and Immunology, Washington University in St. Louis, St. Louis, MO, USA. [4]Department of Pediatrics, Washington University School of Medicine, Saint Louis, MO, USA. [5]Neuroscience Graduate Program, School of Medicine, Washington University in St. Louis, St. Louis, MO, USA.

†These authors contributed equally to this work. *Corresponding author. Email: kipnis@wustl.edu

The meninges are a membranous structure enveloping the central nervous system (CNS) that host a rich repertoire of immune cells mediating CNS immune surveillance. Here, we report that the meninges contain a pool of monocytes and neutrophils supplied not from the blood, but by adjacent skull and vertebral bone marrow. Under pathological conditions, including spinal cord injury and neuroinflammation, CNS-infiltrating myeloid cells can originate from brain borders and display transcriptional signatures distinct from their blood-derived counterparts. Thus, CNS borders are populated by myeloid cells from adjacent bone-marrow niches, strategically placed to supply innate immune cells under homeostatic and pathological conditions. These findings call for reinterpretation of immune-cell infiltration into the CNS during injury and autoimmunity and may inform future therapeutic approaches harnessing meningeal immune cells.

Myeloid cells, including monocytes, neutrophils, and macrophages, display extraordinary heterogeneity and diverse functions depending on their ontogeny and local niche (*1*–*3*). Macrophages represent an essential component of the myeloid niche and take on distinct transcriptional signatures to meet the demands of the tissues in which they reside (*4*). Research on microglia, the macrophages of the central nervous system (CNS), led to the discovery that these tissue-resident macrophages are derived from the yolk sac during embryonic development (*5*–*7*). Unlike several other tissue macrophages that can be replaced by blood-borne monocytes, according to specific anatomical and developmental constraints (*8*), microglia are self-maintained and are not replenished by blood-derived monocytes other than under defined experimental conditions (*5*, *9*–*12*). In such cases, myeloid cells from the periphery may also invade the CNS tissue, although their origin, as well as their stability within the CNS, are poorly understood. The perivascular spaces and the meningeal membranes that cover the borders of the CNS are also populated by a variety of myeloid cells. Based on elegant fate-mapping strategies and multidimensional tools, recent work has begun to reveal the richness of this myeloid landscape, both at steady state and in different diseases (*13*–*20*). Less well studied, however, is the source and role of these brain border-resident monocytes, monocyte-derived macrophages, and neutrophils during homeostasis and CNS dysfunction.

Recent work described the existence of direct ossified vascular channels connecting skull bone marrow to meninges, capable of dispersing neutrophils during inflammation (*21*–*23*). We hypothesized that these connections may also allow homeostatic myeloid trafficking between adjacent meningeal and bone marrow niches. Here, we demonstrate that CNS-associated bone marrow niches in the skull and vertebrae are myeloid reservoirs for the meninges and CNS parenchyma. Under homeostasis, these bone marrow pools supply the brain and spinal dural meninges with monocytes and neutrophils via direct dural–bone marrow connections. Following injury and neuroinflammation, these cells can mobilize to infiltrate the CNS parenchyma, and display distinct phenotypes from their blood-derived counterparts.

Results

CNS borders host a substantial pool of monocytes and neutrophils that are not blood derived

In an attempt to understand the origin of border myeloid cells under homeostasis, we parabiotically joined the circulations of UBC-GFP and wild-type (WT) mice, allowing us to visualize host and fluorescent donor-derived cells, and performed flow cytometric analyses of the blood, brain-associated tissues (cranial dura mater and spinal dura mater), hematopoietic organs (skull bone marrow, vertebrae bone marrow, and femur bone marrow), and peripheral control tissues (spleen and liver) after 60 days of pairing (Fig. 1, A to C). To ensure our analysis only examined true parenchymal

populations and not blood contaminants, mice received intravenous anti-CD45 antibodies 2 min prior to euthanasia, labeling blood and vascular-associated leukocytes that were subsequently excluded in our gating strategy (Fig. 1B). Analysis of WT parabionts demonstrated that although blood chimerism for total CD45$^+$ cells reached a 50:50 ratio (fig. S1A), neither neutrophils nor monocytes ever reached perfect chimerism in the blood. After 2 months, a GFP:WT cell ratio of ~30:70 was achieved (Fig. 1, D and E). The reduced chimerism of these myeloid cells was likely due to the short half-life of these cells as well as active myelopoiesis occurring in the bone marrow.

Despite imperfect blood chimerism of Ly6C$^+$ monocytes and neutrophils, GFP$^+$ cell proportions detected in the cranial dura and spinal dura were significantly lower than that of blood (Fig. 1, D and E). By comparison, the myeloid chimerism displayed in other peripheral tissues were more akin to the proportions present in the blood (Fig. 1, D and E). These data suggested that there was a substantial pool of monocytes and neutrophils located along the brain borders that had not originated from the UBC-GFP parabiont. Cranial and spinal dural CD4 T cells from the UBC-GFP parabiont were not significantly different from the blood chimerism, suggesting a blood origin as described previously (*24*) (Fig. 1F). Furthermore, GFP$^+$Ly6c$^-$ monocytes and B cells displayed different levels of chimerism in distinct tissues. GFP$^+$ B cells specifically appeared to be less represented at the brain borders, also suggesting a non-blood origin (fig. S1, B and C). This phenomenon is described in more detail in an accompanying manuscript (*25*). Additional components of the dural myeloid compartment including macrophages, conventional dendritic cells (cDC)1s, and cDC2s also displayed a low proportion of GFP$^+$ cells compared to the non-border associated spleen pool (fig. S1, D to F). Analysis of several bone marrow niches confirmed that the majority of detected LSK (lineage$^-$SCA-1$^+$c-Kit$^-$) hematopoietic progenitors were GFP$^-$ cells, as expected from an active WT proliferative niche (fig. S1G). We corroborated these flow cytometry data by immunohistochemistry (IHC) and demonstrated only a minor proportion of GFP$^+$CCR2$^+$ and GFP$^+$Ly-6B.2$^+$ cells in WT host tissues (Fig. 1G). Utilizing CD45.1 and CD45.2 pairs as parabionts, we observed a similar imbalance toward host-derived monocytes and neutrophils within the dura compared to the blood chimerism, suggesting the observed findings were consistent across different parabiotic pairs (fig. S1, H and I). Thus, a substantial pool of non-blood-derived monocytes and neutrophils appear to populate the cranial and spinal dura.

Next, we investigated whether the dura harbored monocyte progenitor cells that could maintain a local monocyte pool. Using flow cytometry, we could efficiently identify monocyte–dendritic cell progenitors (MDPs) and monocyte-committed progenitors (cMoPs) in the skull bone marrow. These populations were entirely absent from the cranial dura however (fig. S1, J to S). To exclude the possibility that the low levels of meningeal chimerism observed for Ly6C$^+$ monocytes and neutrophils could be attributed to the proliferation and self-renewal of those cells in the tissue, we explored the turnover of these myeloid cells using a tamoxifen-inducible fate-mapping Cre recombinase system driven by the pan-myeloid promoter LysM to express the fluorescent protein ZsGreen (Fig. 1H). Following tamoxifen injections over 3 consecutive days, blood monocytes and neutrophils reached a recombination efficiency of 36% and 87%, respectively. After 30 days, almost no circulating ZsGreen$^+$ cells could be detected (Fig. 1, I to K). Notably, the fate-mapping efficiency of the blood was mirrored by that in the dura across all investigated time points, indicating that the half-lives of the myelomonocytic cells in the blood and in the meningeal spaces were comparable (Fig. 1, H to K, and fig. S2, A to D). To rule out the possibility that the unlabeled fraction of monocytes and neutrophils provides a local pool of self-sustaining tissue-resident cells, we performed in vivo EdU labeling and K_i-67 staining. Analysis of the blood, cranial dura, and skull bone marrow confirmed that 24 hours after two EdU pulses, the majority of Ly6C$^+$ monocytes and neutrophils in the dura incorporated EdU, but displayed low levels of K_i-67 (fig. S2, E to J). Thus, these cells appeared to originate from a proliferating source, but likely experienced rapid turnover in these tissues and low proliferation capabilities outside the bone marrow niche. Moreover, dural neutrophils displayed the same level of EdU incorporation as the skull bone marrow pool, whereas blood neutrophils were almost entirely devoid of EdU$^+$ cells, suggesting dural neutrophils may arise from the nearby bone marrow sources (fig. S2, E to J). Finally, we investigated if the dural Ly6C$^+$ monocyte and neutrophil pool used meningeal lymphatics to egress from the tissues. For this, we used KikGR transgenic mice with KikGreen-to-KikRed photoconvertible fluorescent protein (*26*). Although neutrophils and Ly6C$^+$ monocytes were present in the draining deep cervical lymph nodes 24 hours after the final photoconversion, no significant differences in KikRed cells could be detected in the deep cervical lymph nodes, compared to unconverted controls (fig. S2, K to N). Thus, replenishment of dural meningeal Ly6C$^+$ monocytes and neutrophils appear to come from a local source and is not due to homeostatic maintenance within the tissue itself or from the blood.

Skull bone marrow supplies brain borders with myeloid cells

Direct connections between the skull and the dura through ossified channels harboring blood vessels extend from the bone marrow to the CNS and allow neutrophils and tumor cell migration during inflammatory or pathological states (*21–23*). One prior strategy for neutrophil tracking utilized

injections into skull bone marrow to label brain-infiltrating cells (*21*). However, on reproducing this approach in an attempt to assess a bone marrow origin for homeostatic dural myeloid cells, we found it unsuitable for this purpose as it resulted in immediate leakage of the tracers into the dura mater and their subsequent drainage by meningeal lymphatic vessels (fig. S3, A to N). Despite the caveats that come with these direct bone marrow injections, we found that a brief topical application of AMD3100, a CXCR4 antagonist, to cranial bone marrow exposed by skull thinning, promoted myeloid cell egress. This resulted in significant elevations in Ly6C$^+$ monocytes and neutrophils in underlying dura mater, without altering proportions in the blood, lung, or other bone marrow niches, suggesting direct migration from local skull bone marrow (Fig. 2, A to E). We did not observe a change in the number of myeloid cells in the skull bone marrow 24 hours following AMD3100 administration. This is likely due to the number of monocytes and neutrophils infiltrating the dura representing only a very small proportion of the CNS-associated bone marrow niche.

These data prompted us to look closely into the possibility that the skull bone marrow is a source for meningeal myeloid cells. Therefore, we developed a calvaria bone-flap transplantation, in which a piece of the calvarium (~6×4 mm) containing a substantial bone marrow reservoir was transplanted from UBC-GFP mice to cover a skull window of similar size created in WT mice whose dura mater was carefully left intact (Fig. 2F). IHC analysis of transplanted calvaria flaps 7 and 30 days after transplantation revealed the continued presence of GFP$^+$ bone marrow, though some sites were partially repopulated by non-GFP expressing cells (Fig. 2G and fig. S4, A and B). Consistent with sterile injury-induced dural angiogenesis (*27*), vascular remodeling was observed at 7 days, but returned to the coverage of naive mice after 30 days (Fig. 2H and fig. S4, C and D). The transplanted flap contained cranial sutures necessary for skull repair (*28*). Indeed, after 1 month, transplanted bone was incorporated into the WT skull (fig. S4E and movie S1). We detected GFP$^+$ cells including CCR2$^+$ monocytes, IBA1$^+$ macrophages, and CD31$^+$ vasculature in the underlying dura of the transplanted calvaria flap (fig. S4, F and G). Flow cytometric analysis of blood, cranial dura, and skull bone marrow confirmed that although the donor pool of GFP$^+$ cells in the transplanted skull bone marrow niche was low, it was able to give rise to dural Ly6C$^+$ monocytes and neutrophils even 30 days posts transplant (Fig. 2, I to M, and fig. S4, H and I). Demonstrating a direct route for dural myeloid infiltration from the transplanted skull, we observed previously described vascular channels connecting the transplanted skull to the dura mater (fig. S4, J and K, and movies S2 and S3). Analysis of the underlying cortex revealed no microglial activation via Sholl analysis after 30 days (fig. S4, L and M) and following an initial weight loss after transplantation, mice resumed a normal weight gain, suggesting minimal chronic perturbations using this model (fig. S4N).

We next used an irradiation regime to further exclude the possibility that the observed phenotype following parabiosis or calvaria bone flap transplantation strategies is inflammation driven (Fig. 2N). Mice underwent lethal irradiation coupled with different shielding strategies and were reconstituted with UBC-GFP-derived bone marrow. As expected, cranial dural Ly6C$^+$ monocytes and neutrophils in head-shielded mice, whose bodies were irradiated, showed similar levels of chimerism as skull bone marrow. Chimerism at both sites were significantly lower than the blood and femur bone marrow (Fig. 2, O to Q). The body-shielding strategy, in which the head was irradiated, displayed the opposite effect with a significantly higher proportions of GFP$^+$ cells in the skull bone marrow and cranial dura, compared to blood or femur bone marrow (Fig. 2, R and S).

To explore dural-derived factors that could recruit bone marrow-derived myeloid cells, we utilized RNA-magnet algorithms from whole dura single-cell RNA sequencing (scRNA-seq) analysis (*24*), to unbiasedly identify ligand expression for monocyte and neutrophil chemokine receptors (fig. S5, A and B). We then performed semiquantitative chemokine protein expression analysis from whole dura homogenates, to confirm the true presence of predicted ligands (fig. S5C). We identified high expression of CCL2, CCL12, and CCL8, which can recruit monocytes through CCR2 signaling as well as CCL6, which can recruit neutrophils via CCR1. This suggested that the homeostatic dura contains appropriate signals for local myeloid recruitment from adjacent bone marrow (fig. S5, C to E). Thus, under homeostatic conditions, the myeloid niche distributed along the brain borders receives a substantial input from the skull bone marrow, which appears to act as a critical dispenser of myeloid cells. This provides an example of a healthy tissue hosting myeloid cells that are continuously replenished by a source that does not use blood as a major route.

The inflamed CNS is infiltrated by blood and CNS-adjacent bone marrow-derived myeloid cells

Intrigued by the large proportion of non-blood-derived monocytes and neutrophils residing in the dura, we speculated that these cells may be positioned for a prompt response in the event of parenchymal CNS damage. We proceeded to investigate this scenario using parabiotic pairing in three CNS-injury models, experimental autoimmune encephalomyelitis (EAE), spinal cord injury, and optic nerve crush injury. For EAE experiments, WT and UBC-GFP mice were joined parabiotically for 60 days and both groups were immunized with myelin oligodendrocyte glycoprotein (MOG) peptide (35-55) in complete Freud's adjuvant (CFA) to induce EAE. Lumbar

spinal cord, lumbar vertebral bone marrow, spinal dura, and blood were collected from the WT parabionts 15 days after EAE induction and stained for flow cytometry and IHC (Fig. 3A and fig. S6, A and B). In agreement with their homeostatic presence, a substantial pool of dural and CNS-infiltrating Ly6c$^+$ monocytes did not originate from the blood, indicated by their significantly lower GFP$^+$ proportion compared to the blood chimerism (Fig. 3, B and C). Interestingly, the same was not observed for neutrophils, CD4 T cells, and Ly6C$^-$ monocytes, suggesting blood as the major source of these infiltrates at this time point (Fig. 3D and fig. S6, C to E). Dural and spinal cord GFP$^+$ macrophages were also observed, suggesting infiltrating monocytes can differentiate under these inflammatory conditions, though not at a sufficient amount to explain the chimerism discrepancy (fig. S6F). In agreement with flow cytometry analysis, IHC for cranial dura, spinal dura, and spinal cord, revealed that infiltrating GR1$^+$ cells within WT tissues were rarely GFP$^+$ (Fig. 3E). In the cranial dura, GR1$^+$ cells were mostly associated with the dural sinuses, and we observed evidence of intraluminal lymphatic localization, suggesting the possibility of lymphatic trafficking of myeloid cells during neuroinflammatory diseases as previously described (*29*) (fig. S6, G to I).

Following spinal cord injury in CD45.1–CD45.2 parabionts, CNS-infiltrating Ly6C$^+$ monocytes (but not neutrophils, CD4 T cells, or Ly6C$^-$ monocytes) also displayed a significantly lower proportion of host-derived cells in the spinal cord and spinal dura compared to blood, suggestive of a local bone-marrow origin (fig. S7, A to G). GFP$^+$ monocyte-derived macrophages were present, but their proportion in the injured spinal cord was low (fig. S7H). Similar results were obtained for another CNS injury, whereby optic nerve infiltrating Ly6C$^+$ monocytes and neutrophils following optic nerve crush in WT–UBC-GFP parabionts displayed a significantly lower proportion of donor-derived cells compared to the blood chimerism (fig. S7, I to L). Importantly, the same was not observed in a periphery injury model utilizing ear skin puncture that lacks a local bone-marrow reservoir and shows similar chimerism in the site of injury to that observed in the blood (fig. S7, M to P).

To identify a direct route allowing non-blood-derived monocytes to invade spinal cord tissue, we explored whether bone marrow channels identified for the skull were present in spinal cord vertebrae. Using H&E staining and IHC in naive and EAE mice 15 days post induction, we observed channels directly connecting vertebrae bone marrow to spinal dura, with cells present within the channels (Fig. 3F and fig. S8, A to C). Further, we observed that spinal cord infiltrates of GR1$^+$ cells were frequently associated with the presence of these bone marrow–spinal dura channels (Fig. 3F). The exact anatomical connections of these channels remain controversial, but we found that channels terminated within the dura mater and did not directly contact the CNS tissue (Fig. 3F and fig. S8, A to C). Exactly how myeloid cells traverse the underlying arachnoid and pia maters to penetrate the CNS parenchyma remains to be established, but like the blood–brain barrier, it is plausible that these barriers, consisting of tight junctions, are similarly disrupted under neuroinflammatory conditions (*30*).

We next sought to determine whether CNS-infiltrating monocytes of different origins (i.e., blood versus bone marrow/meningeal), may have different phenotypes based on the route by which they gain access to the CNS. To explore this, we induced EAE in WT–UBC-GFP parabionts, and isolated GFP$^+$ and GFP$^-$ spinal cord-infiltrating IV-CD45$^-$CD45^{hi} cells from WT mice 15 days post induction, and performed scRNA-seq (fig. S9, A to C). The majority of sorted cells were monocytes, but we also obtained populations of neutrophils, dendritic cells (DCs), B cells, T cells, microglia/macrophages, and an undefined proliferating population cluster of cells from both GFP$^+$ and GFP$^-$ populations (Fig. 3, G and H). In agreement with previous EAE experiments, monocytes made up the majority of the GFP$^-$ pool, consistent with a non-blood origin (Fig. 3I and fig. S9C). Gene ontology pathway analysis for biological processes of differentially expressed genes in GFP$^+$ versus GFP$^-$ monocytes revealed down-regulated pathways involved in anion and lipid transport metabolism pathways and wound healing (Fig. 3J and table S1). Up-regulated pathways were largely involved in leukocyte migration, adhesion, and T cell activation (Fig. 3K and table S1). Analysis of differentially expressed genes revealed a significant induction of diverse myeloid and lymphocyte chemokines (*Ccl2*, *Ccl5*, *Cxcl9*, and *Cxcl16*) and pro-inflammatory cytokines (*Il6*, *Il1a*, *Il1b*, *Tnf*, and *Ifng*) (Fig. 3L and table S2). These data suggest a potential skewed pro-inflammatory role for blood compared to bone marrow-derived monocytes in EAE, in line with the recently described pathogenic subset of CXCL10$^+$/CXCL9$^+$ monocytes in neuroinflammatory disease (*31*). These cells may be involved in enhanced leukocyte trafficking, for example by CCL5-, CXCL9-, and CXCL16-mediated T cell recruitment and proinflammatory cytokine production, which are critical factors in EAE pathogenesis (*32*).

Notably, scRNA-seq analysis of infiltrating IV-CD45$^-$CD45^{hi} GFP$^+$ versus GFP$^-$ monocytes from the spinal cord of WT parabionts 3 days post spinal cord injury, revealed a similar up-regulation of pathways involved in leukocyte migration and activation, with several conserved up-regulated chemokines and cytokines in GFP$^+$ blood-derived monocytes (fig. S9, D to L, and tables S3 and S4). Thus, there may be differential roles in blood versus bone-marrow-derived monocytes in diverse CNS injury and inflammatory conditions, perhaps similar to those observed for choroid plexus compared to blood trafficking during spinal cord injury (*33*).

Discussion

In this study, we demonstrate that the steady-state myeloid niche located at the CNS borders in mice consists of a substantial pool of monocytes and neutrophils that are continuously replenished from bone-marrow niches in the adjacent skull or vertebrae. Our model of calvaria bone-flap transplantation—used here as a proof-of-concept prototype—and various irradiation regimes demonstrate that skull bone marrow can supply the adjacent meningeal tissue with myelomonocytic cells without using the blood route. Moreover, our results indicate that these bone-marrow-derived monocytes can differentiate into meningeal macrophages. This revealed a myeloid niche that is open to homeostatic peripheral inputs that, in contradiction to the classic Van Furth dogma, does not use the blood as a major route.

It is tempting to speculate that channels aligned between the bone marrow and the dura might, under homeostatic conditions, represent a principal route for the migration of monocytes and neutrophils. In our skull transplantation model, we detected GFP^+ vascular elements sprouting from the bone-marrow niche and extending toward the dural parenchyma. It is therefore reasonable to conceive of a scenario wherein myelomonocytic cells crawl abluminally along these vessels using the vasculature as a scaffold, as is the case of neuroblasts during CNS development (*34*), glioma tumor spread in the brain parenchyma (*35*), or T cells finding their zone in the spleen (*36*).

Beyond homeostatic trafficking, we demonstrated that in the context of either injury or autoimmune neuroinflammation, monocytes can invade the brain and spinal cord parenchyma without the need for blood, and thus breakdown of the blood–brain barrier. In this sense, the brain seems to behave as a unique organ, in that it is able to hold a privileged dialogue with its surrounding tissues. Indeed, we envisage these monocytes and neutrophils as a myeloid reservoir situated at the borders of the CNS under homeostatic conditions and ready to leap to its defense when needed, thereby complementing blood-borne inflammatory cells in supporting the CNS. Whether dura-derived chemokines differentially favor migration from local bone marrow over blood, or indeed whether the two routes use different recruitment factors entirely remains to be clarified. Intriguingly, this could allow for the manipulation of specific subsets of myeloid cells, with potentially unique phenotypes. From our scRNA-seq analysis, it appears that infiltrating $Ly6c^+$ cells from the blood and the bone marrow may have distinct roles in EAE pathology, potentially through differences in immune cell recruitment or exacerbation of inflammatory events, though the exact participation remains to be seen. It will also be intriguing to further explore the kinetics of blood-and CNS-associated bone marrow-derived myeloid infiltration during EAE development, to explore whether one population represents the "first responders" to CNS disruption.

The skull and vertebral bone-marrow-derived meningeal myeloid reservoir described here reshapes our interpretation of the neuroimmunological events occurring at the CNS borders under both physiological and pathological conditions. It appears likely that this reservoir of immune cells may also be of relevance in other scenarios of brain pathology, such as neurodegeneration, brain tumors, CNS or meningeal infection, and aging, or in the context of microglial replacement under specific ablative regimens.

Materials and methods

Mice

Mice were housed in the animal facility 4-to-5 animals per cage in a temperature and humidity-controlled environment with a 12-hour light–dark cycle. Mice were provided with rodent chow and water ad libitum. All mice were housed for habituation for at least 1 week before the start of the experimentation. Unless specified otherwise, mice were 2-3 months of age at the beginning of the experiments. The following strains were used: C57BL/6 (WT; JAX 000664), C57BL/6-Tg(UBC-GFP)30Scha/J(UBC-GFP; JAX 004353), B6.SJL-Ptprca Pepcb/BoyJ (CD45.1; JAX 002014), Lyz2 tm1(CRE^{ER-T2})Grtn/J (LysM-CRE^{ER-T2}; JAX 031674), B6.Cg-Gt(ROSA)26Sor tm6(CAG-ZsGreen1)Hze/J (Zsgreen, JAX 007906), Prox1-CRE^{ER-T2} (JAX 022075), B6.Cg-Gt(ROSA)26Sor tm14(CAG-tdTomato)Hze/J (Ai14; JAX 007914),) Tg(CAG-KikGR)33Hadj/J (KikGR, JAX 013753). Mice were bred in house or purchased from the Jackson Laboratory. All experiments were approved by the Institutional Animal Care and Use Committee of the University of Virginia and/or Washington University in St. Louis. Experiments were only performed in institutions for which experimental approval was granted.

Parabiosis

Mice were anesthetized with an intraperitoneal injection of a ketamine (100 mg per kilogram)–xylazine (10 mg per kilogram) cocktail. Fur was shaved on the corresponding lateral aspect of each mouse and cleaned with alternating Betadine solution and alcohol swabs. After muscles were fully relaxed, matching skin incision from the olecranon to the knee joint was made on each side of the incision, the subcutaneous fascia was bluntly dissected to create 0.5 cm of free skin. To reduce direct pulling on the skin sutures, the olecranon and knee were sutured together by an absorbable 5-0 Vicryl suture. After pressing together, the dermis of the parabiotic partners, skins incisions were closed with 5-0 Nylon suture. Post-surgery, systemic analgesics (2.5 mg of ketoprofen per kilogram) and antibiotics (2.5 mg of Baytril (Bayer) per kilogram) were administered. One single parabiotic pair was housed per cage, wet food was provided, and mice were monitored daily for pain and distress. Unless specified otherwise,

all parabiotic pairs were sacrificed after 60 days, disjoined, and separately perfused.

Tissue collection and processing for immunohistochemistry

Mice were sacrificed using a lethal dose of anesthetics (Euthasol, 10% v/v) via IP injection and transcardially perfused with 0.025% heparin in PBS solution. Cranial meninges and brain were harvested by immediate decapitation posterior to the occipital bone; skin, mandible and muscles were removed, and skull was fixed in 4% paraformaldehyde (PFA) at 4°C for 24 hours. After 24 hours, the meninges were peeled from the skull cup and placed in PBS with 0.25% sodium azide at 4°C until used. Brains were fixed for additional 24 hours in PFA at 4°C, transferred in PBS with 30% sucrose until fully immersed and then embedded in OCT compound (Fisher), frozen rapidly over dry ice, and stored at −20°C until use. Forty-micrometer-thick sections (coronal) were sliced on a cryostat (Leica). Calvarium and femur were fixed in 4% PFA at 4°C for 24 hours, transferred in decalcification solution (PBS with 0.1 M of EDTA) at agitation for 4-6 days at 37°C with daily change of the solution, and then transferred in PBS with 30% sucrose overnight. Calvarium and femur were then embedded in OCT, frozen rapidly over dry ice and stored at −20°C until use. Thirty-micrometer-thick sections (coronal or sagittal) were sliced onto gelatin-coated slides on a cryostat (Leica). Vertebral laminae were cut on both sides, vertebral foramen was exposed, and spinal cord was dissected using fine forceps and fixed in 4% PFA at 4°C for 48 hours. Meninges were cut along the ventral side and whole-mount meninges were peeled from spinal cord and placed in PBS with 0.25% sodium azide at 4°C until used. Spinal cord was transferred in PBS with 30% sucrose overnight, embedded in OCT, frozen rapidly over dry ice and stored at −20°C until use. Twenty-five-micrometer-thick sections were sliced onto gelatin-coated slides on a cryostat (Leica). Liver, lung, and lymph nodes were harvested using forceps, placed in 4% PFA overnight, transferred into PBS containing 30% sucrose overnight and then embedded in OCT and frozen rapidly over dry ice and stored at −20°C until use. Twenty-five-micrometer-thick sections were sliced onto gelatin-coated slides on a cryostat (Leica). For immunofluorescence staining, tissues were rinsed in PBS and washed with PBS with 0.2% Triton X-100 for 10 min, followed by incubation in blocking and permeabilization buffer containing PBS with 0.2% Triton X-100 and 2% normal chicken serum for 1 hour at room temperature with gentle agitation. If applicable, endogenous biotin was blocked using streptavidin/biotin blocking kit (Vector Laboratories SP-2002) following manufacturer's instructions. To quench autofluorescence of femur and skull bone marrow, Trueblack (Biotium, 23007) was used following manufacturer's instructions. Sections were then incubated with primary antibodies in the blocking and permeabilization buffer for 24 hours at 4°C with gentle agitation, washed three times with PBS with 0.2% Triton X-100, and incubated with secondary antibodies in blocking and permeabilization buffer for 2 hours at room temperature. Slices were washed three times with PBS containing 0.2% Triton X-100 and nuclei were then counterstained with DAPI. Free-floating sections were mounted on Superfrost Plus slides and coverslipped with Aqua-Mount (Lerner) or ProLong Gold Antifade Mountant (Molecular Probes) and glass coverslips. Gelatin-coated slides were mounted with Aqua-Mount (Lerner) and glass coverslips.

For H&E staining, formalin fixed spines were embedded in paraffin and 10-μm-thick sections were cut on a microtome (Leica), mounted onto slides, deparaffinized, and stained with Hematoxylin and Eosin Stain Kit (Vector Laboratories H-3502) according to the manufacturer's instructions.

For cleared skull-dura whole-mount imaging, the vDISCO tissue clearing and processing protocol was used as described (*23*). Briefly, after perfusion, skull with attached meninges was dissected, placed in PBS 4% PFA overnight, followed by decolorization solution for 24 hours. After washing with PBS, samples were placed in decalcification solution (10 wt/Vol% EDTA (Carl Roth, 1702922685) in 0.1 M PBS) for 2 days at room temperature. Samples were then permeabilized, stained, and cleared using the vDISCO protocol with passive tissue immersion as described (*23*). Cleared samples were immersed in ethyl cinnamate (Sigma, W243019) and placed in chambered cover-glass (Thermo, 155360) for imaging.

Confocal microscopy and image analysis

Tissues slides were stored at 4°C for no more than 1 week until images were acquired using confocal microscopy (Leica, TCS SP8 or Leica, Stellaris) with 10X (0.4 NA), 20X (0.75 NA), and 40X (1.3 NA) objectives (Leica) and widefield microscopy (Olympus Slideview VS200) with 10X (0.4 NA), 20X (0.8 NA), and 40X (0.95 NA) objectives (Olympus) and a Hamamatsu ORCA Flash4.0 V3 digital camera. Quantitative analysis of acquired images was performed using Fiji package for ImageJ. Five-to-fifteen representative images were acquired per sample and the results were averaged to generate the value utilized for a single mouse.

Single-cell isolations

Mice were injected with a lethal dose of Euthasol (10% vol/vol) and transcardially perfused with ice-cold PBS with 0.025% heparin. Blood was collected before perfusion from the retroorbital sinus. Blood was centrifuged at 420*g* for 4 min. Red blood cell lysis was then performed by resuspension in 1 ml of ACK lysis buffer (Quality Biological) for 10 min at room temperature, and 2 ml of PBS was added to inactivate ACK buffer. After centrifugation at 420*g* for 4 min samples

were resuspended in FACS buffer (PBS with 2% BSA) and kept at 4°C until use. Tissues were harvested as described above. Briefly, dura and lymph nodes were digested for 15 min and lung, liver, and skin were digested for 30 min at 37°C in pre-warmed digestion buffer (DMEM with 1 mg/ml Collagenase VIII (Sigma-Aldrich) supplemented with 0.5 mg/ml of DNase I (Sigma-Aldrich), 2% FBS). After digestion tissues underwent several steps of mechanical homogenization followed by filtration through a 70-μm cell strainer. Enzymes were inactivated with DMEM with 10% FBS and cells were then centrifuged at 420*g* for 4 min and washed in FACS buffer. Single-cell suspensions were kept in FACS buffer on ice until use. After dissecting the meninges, spinal cord and brains were harvested, followed by digestion step for 30 min in pre-warmed digestion buffer, triturated with a 10-ml serological pipette, digested for an additional 20 min and again triturated with a 5-ml serological pipette. Cells were passed through a 70-μm cell strainer, enzymes were inactivated by adding an equal volume of DMEM with 10% FBS and samples were centrifuged at 420*g* for 4 min. Myelin was removed by adding a 1:1 ratio of 22% BSA in PBS to DMEM and samples were centrifuged at 1000*g* for 10 min, with no brake. The upper myelin-containing layer and underlying BSA was aspirated and the single-cell suspension was kept in FACS buffer until use. For the isolation of skull bone marrow, meninges were peeled from skull cup as described above. The calvarium was then cut into small pieces using sterile scissors and mechanically dissociated in FACS buffer with a pestle, followed by a filtration step through a 70-μm cell strainer. After centrifugation at 420*g* for 4 min, red blood cells were removed by adding 1 ml of ACK lysis buffer for 2 min at room temperature, centrifugation at 420*g* for 4 min, and the cell pellet was resuspended in FACS buffer until use. Femur bone marrow was harvested by dissecting the left femur. The proximal and distal epiphysis were cut using sterile scissors and bone marrow was then flushed out from the femur using a 23G needle filled with PBS with 2% BSA onto a 70-μm cell strainer and gently pressed. After centrifugation, red blood cells were lysed with 1 ml ACK lysis buffer for 2 min, centrifuged at 420*g* for 4 min, and resuspended in ice-cold FACS buffer until use.

Flow cytometry and fluorescence-activated cell sorting

Single-cell suspensions were washed and resuspended in FACS buffer. FC receptors were blocked for 5 min on ice using an anti-CD16/CD32 antibody cocktail (FC block; 2 μg/ml, Biolegend), followed by a 10-min incubation at room temperature with antibody cocktails for surface staining. The list of flow antibodies is provided in table S5. To determine cell viability, Zombie Aqua or Zombie NIR fixable Viability kit was used following the manufacturer's instructions. Samples were acquired with a Gallios flow cytometer (Beckman Coulter) or an Aurora spectral flow cytometer (Cytek). Data were analyzed using FlowJo version 10. For FACS a BD FACSAria II (BD Biosciences) was used.

IV immune labeling

To label intravascular leukocytes, mice were retro-orbitally injected with 2 μg of PE-conjugated anti-CD45 antibody (Biolegend, clone 30-F11) under isoflurane anesthesia 2 min before euthanasia. In all instances, proper IV administration was confirmed by complete labeling of blood leukocytes.

Tamoxifen-induced Cre recombination

To induce Cre recombination in LysmCreER^{T2} mice, a 20 mg/ml stock solution of tamoxifen (Sigma Aldrich) was prepared by dissolving in corn oil at 37°C for 24 hours followed by sterile filtration. Transgenic mice were injected IP daily with 100 μl of tamoxifen at 8 weeks of age for 3 consecutive days. Mice were then sacrificed at 0, 3, 14, or 30 days after the final tamoxifen injection.

Intracalvaria and intratibial bone marrow injection

All procedures were performed on mice anesthetized with a ketamine (100 mg per kilogram)–xylazine (10 mg per kilogram) mixture. Body temperature was maintained throughout the surgery by placing mice on a heating pad at 37°C while they were restrained in a stereotaxic apparatus. The head of the mouse was shaved, a skin midline incision was made, and the skull was exposed. Injections were performed similarly as described previously (*21*). Briefly, an electric drill was used to gently erode the compact bone covering bone marrow niches on occipital and frontal bones until a thin layer of periosteum was left. A Hamilton syringe complemented with a 34G-blunt needle- RN 0.37 PT3 was used to manually poke the final hole for the injection. All injections were performed manually. Every injection consisted of a maximum volume of 2 μl. A single injection took around 45 s. After the injection the needle was maintained in place for 15 s in order to prevent excessive leakage of the injected solution. Several injections were performed per mouse for a total final volume injected that ranged between 4 μl and 10 μl. Several types of injections were performed: (a) UBC-GFP progenitor cells freshly flushed from femur (roughly 10,000 cells injected per mouse); (b) Evans Blue; (c) CD45-PE antibody (Biolegend, clone 30-F11); and (d) CellTracker Deep red (C34565, Molecular Probes). The Hamilton was filled directly with the concentrated antibody solution from the Biolegend/Molecular Probes vials. For intratibial bone marrow injection, a skin incision was made below the knee and using a 30G needle bone was perforated between tuberosity and crest of tibia. Three microliters of CellTracker CMFDA (green) (C7025 Molecular Probes) dye was manually injected over 30 s. After the procedure, the skin was sutured and mice were gently placed on a heating pad and monitored until awake. Once awake, mice

were injected with Ketoprofen and antibiotics (enrofloxacin, 2.5 mg per kilogram). After the bone marrow injections, mice were sacrificed 2 or 24 hours later.

Skull bone marrow delivery of AMD3100 was performed as previously described (*37*). Briefly, mice were anesthetized with a ketamine (100 mg per kilogram)–xylazine (10 kg per kilogram) mixture. The head of the mouse was shaved, a skin midline incision was made and skull was exposed. Using an electrical drill, the outer periosteal layer was thinned on top of skull bone marrow near the bregma and lambda on five spots, without damaging the bone marrow. One microliter of 1 mg/ml AMD3100 (ab120718, Abcam) or vehicle was applied on each spot for 5 min. The skin was sutured and mice were sacrificed 24 hours later.

Calvarium bone flap transplantation

Mice were anesthetized with a ketamine (100 mg per kilogram)–xylazine (10 mg per kilogram) mixture. Body temperature was maintained throughout the surgery by placing mice on a heating pad at 37°C. The heads of WT mice were shaved, skin midline incisions were made, and the skull was exposed. Using an electrical drill, a 4×6 mm cranial window was made on parietal and interparietal bones. During bone drilling, periodic pauses were made to cool the bone with 0.9% sodium chloride solution. After the cranial window was detached from surrounding bones, craniotomy was performed with the help of fine forceps, extra caution was made not to damage the underlying dura mater. Craniotomy was performed with abundant 0.9% sodium chloride solution bathing the brain. If dura mater, brain, or sinuses were damaged during the craniotomy, mice were sacrificed and were not used for our analysis. In parallel, a sex-matched UBC-GFP mouse, whose skull bone marrow was used as a donor of calvarium, was euthanized, decapitated, and a piece of calvarium comparable to the window drilled in the host mouse was obtained. Connective tissue and pericranium layers were left attached on the bone flap to increase survival of the transplanted bone. Before the transplantation, meninges were peeled from the donor skull. The donor piece of skull containing the bone marrow was carefully placed within the surgical window created in the host mouse. Then, the donor skull was fixed to the host skull using cyanoacrylate glue and a trimmed 10-0 nylon suture needle. The skin was sutured and mice were maintained on a heating pad until they awoke. Mice were observed daily and injected with Ketoprofen (2.5 mg per kilogram) and antibiotics (2.5 mg of Baytril (Bayer) per kilogram) once per day for the first 5 days after the transplantation day.

Experimental autoimmune encephalomyelitis (EAE)

For active induction of EAE in parabiotic pairs, both mice joined in parabiosis were immunized by subcutaneous injection of 200 μg of MOG35–55 (CSBio) in complete Freund's adjuvant (Sigma Aldrich) with 4 mg/ml of *Mycobacterium tuberculosis* (H37Ra) (BD Biosciences). Mice received 200 ng of pertussis toxin (List Biological Laboratories) IP on day 0 (immunization day) and day 1 (24 hours after immunization).

Spinal cord injury

Mice were anesthetized with a ketamine (100 mg per kilogram)–xylazine (10 mg per kilogram) mixture. Skin over the upper thoracic area was shaved and cleaned with betadine and alcohol. A 15-mm midline skin incision was made, and connective tissue and muscles were bluntly dissected. After a Th9 laminectomy the spinal cord was crushed with fine forceps. After the injury, muscles and skin were sutured separately and allowed to recover from anesthesia on heating pads. Once awake mice were injected daily intraperitoneally with buprenorphine (0.05 mg per kg) and Baytril (2.5 mg per kilogram) (Bayer) for 3 consecutive days. Seventy-two hours after surgery, mice were sacrificed for further analysis.

Skin injury

Mice in parabiosis were briefly anesthetized by placing them in an isoflurane induction chamber for 3 min, then a fast ear punch was performed on the left ear of each parabiont (WT and UBC-GFP mouse). The ear puncher was cleaned with a solution of 70% ethanol between each couple of parabionts. After the punch, mice were injected intraperitoneally with Ketoprofen analgesia (2.5 mg per kilogram) and placed back in their cages to wake. Mice were sacrificed 24 hours following skin injury.

Optic nerve injury

Mice in parabiosis were anesthetized by placing them in an isoflurane induction chamber for 3 min. The soft tissue around the eye was dissected to expose the optic nerve. The optic nerve was crushed with an N5 self-closing forceps. Mice were injected intraperitoneally with Ketoprofen analgesia (2.5 mg per kg), placed back in their cages, and allowed to recover on a heating pad. Mice were sacrificed 24 hours following optic nerve injury.

Irradiation and bone marrow transplantation

All mice received split dose irradiation with a first dose of 550 rad (5.5 Gy) followed by another dose of 550 rad (5.5 Gy) 6-7 hours later. For full body irradiation mice were irradiated without anesthetics. For head shielding, mice were anesthetized with a ketamine (100 mg per kilogram)–xylazine (10 mg per kilogram) mixture. Mice heads were shielded using 1-inch-thick lead shield (1 inch Lead Vial Shield, 50 ml, Pinestar Technology), exposing the body below the neck. Alternatively, for body shielding, mice were inserted into a lead shield exposing only the head. All mice were injected IV with 4×10^6 (100 μl in PBS) freshly isolated bone marrow cells from UBC-

GFP donors 6 hours after the last irradiation. Mice were analyzed 4 weeks after the bone marrow transplantation.

EdU and Ki67 staining for proliferation analysis

Mice received two intraperitoneal injections of 10 mg of EdU per kilogram 24 hours apart and were sacrificed 24 hours after the final injection. After generation of single-cell suspensions for flow cytometry and surface staining as described earlier, fixation, permeabilization, and EdU staining was performed following manufacturer's instruction (Click-iT Plus EdU Alexa Fluor 488 Flow Cytometry Assay Kit, C10632, ThermoFisher Scientific). Intracellular staining for Ki67 and additional staining for PE conjugates was performed for 10 min at room temperature following EdU staining.

Photoconversion of KikGR

Mice were anesthetized with a ketamine (100 mg per kilogram)–xylazine (10 mg per kilogram) mixture. The heads were shaved, skin midline incisions were made, and the skull was exposed. Photoconversion was performed using an Optogenetics-LED-Violet module (Prizmatix) with the light source placed 1 cm above the skull for 2 min at an intensity of 5. Mice were then sutured and allowed to recover on a heating pad until responsive.

Proteome profiler chemokine array

Chemokines were semiquantitatively determined from 2-month-old WT mouse dural homogenates using the Proteome Profiler Mouse Chemokine Array Kit (R&D Systems) as per manufacturer's instructions. Briefly, peeled cranial dura was peeled from the skull and placed into PBS with 1X Complete Mini ETA Protease inhibitor cocktail (Sigma Aldrich) and homogenized using a Mini Beadbeater (BioSpec Products) and 2.3-mm zirconia/silica beads (BioSpec Products). Triton X-100 was added to a final concentration of 1%, samples, samples were frozen at −80°C, thawed, and centrifuged at 1000*g* for 10 min to pellet tissue. Three pooled dural homogenates were used for each sample, and samples were run in duplicate. Semi-quantitative analysis was performed via densitometric measurements using FIJI.

EAE scRNA-seq

Three pairs of female WT and UBC-GFP C57BL/6J mice were parabiotically joined at 2 months of age. Mice were allowed to recover for 60 days, where after experimental autoimmune encephalomyelitis (EAE) was induced in both pairs by MOG35-55 immunization. After 15 days, mice were sacrificed, and spinal cord tissue was collected from the WT parabionts. Tissues were dissociated, stained, and sorted using a BD FACSAria II (BD Biosciences) based on the following phenotypes: $DAPI^{-}CD45^{hi}IV\text{-}CD45^{-}GFP^{-}$ singlets or $DAPI^{-}CD45^{hi}IV\text{-}CD45^{-}GFP^{+}$ singlets. Each sample represents GFP^{-} or GFP^{+} subsets from three pooled female mice at 4-5 months of age. Cells were sorted into 1.5-ml tubes with DMEM, pelleted, viability determined using trypan blue exclusion, and resuspended in 0.04% non-acetylated BSA. Sample loading and library construction were performed using the 10X Genomics Chromium platform and Chromium Single Cell 3′ Library & Gel Bead Kit v3 as previously described (*24*) Data preprocessing, dimensionality reduction and clustering, differential expression analysis, and pathway enrichment were performed as previously described (*24*)

Spinal cord injury scRNA-seq

Four pairs of female WT and UBC-GFP C57BL/6J mice were parabiotically joined at 2 months of age. Mice were allowed to recover for 60 days, where after spinal cord injury was performed in both pairs by a crush at Th9 level with fine forceps. After 3 days, mice were sacrificed, and spinal cord tissue was collected from the WT parabionts. Tissues were dissociated, stained, and sorted using a BD FACSAria II (BD Biosciences) based on the following phenotypes: $DAPI^{-}CD45^{hi}$ IV-$CD45^{-}GFP^{-}$ singlets or $DAPI^{-}CD45^{hi}IV\text{-}CD45^{-}GFP^{+}$ singlets. Each sample represents pooled GFP^{-} or GFP^{+} subsets from four pooled female mice at 4-5 months of age. Cells were sorted into 1.5-ml tubes with DMEM, pelleted, viability determined using trypan blue exclusion, and resuspended in 0.04% non-acetylated BSA. Sample loading and library construction were performed using the 10X Genomics Chromium platform and Chromium Single Cell 3′ Library & Gel Bead Kit v3 as previously described (*24*) Data preprocessing, dimensionality reduction and clustering, differential expression analysis, and pathway enrichment were performed as previously described (*24*)

Whole-dura scRNAseq analysis

Whole-dura scRNA-seq analysis was performed on samples previously described (*24*). To determine potential cell–cell ligand–receptor interactions promoting monocyte and neutrophil infiltration, the RNAMagnet package (*38*) with RNAMagnetSignaling was used and the top signaling pair molecules were examined for both monocytes and neutrophils with every other cell type present in the dataset as previously described (*24*).

Experimental study design

All experiments were blinded, where possible, for at least one of the independent experiments. For irradiation and bone-marrow transfer experiments and skull transplantation studies, blinding was not possible due to obvious differences in the physical appearance of mice. No data were excluded, with the exception of skull transplantation studies, where mice were excluded if they displayed no GFP signal in the skull bone marrow after 7 or 30 days, demonstrating that the

surgery was unsuccessful. Animals from different cages were randomly assigned to different experimental groups. Statistical methods were not used to recalculate or predetermine study sizes but were based on similar experiments previously published (*24*, *39*, *40*, *41*). Statistical tests for each experiment are provided in figure legends. All data represent biological replicates. Statistical analysis was performed using Prism 8.0 (GraphPad Software Inc.).

REFERENCES AND NOTES

1. K. Bassler, J. Schulte-Schrepping, S. Warnat-Herresthal, A. C. Aschenbrenner, J. L. Schultze, The myeloid cell compartment—Cell by cell. *Annu. Rev. Immunol.* **37**, 269–293 (2019). doi:10.1146/annurev-immunol-042718-041728 Medline
2. M. Guilliams, A. Mildner, S. Yona, Developmental and functional heterogeneity of monocytes. *Immunity* **49**, 595–613 (2018). doi:10.1016/j.immuni.2018.10.005 Medline
3. L. G. Ng, R. Ostuni, A. Hidalgo, Heterogeneity of neutrophils. *Nat. Rev. Immunol.* **19**, 255–265 (2019). doi:10.1038/s41577-019-0141-8 Medline
4. S. Gordon, A. Plüddemann, Tissue macrophages: Heterogeneity and functions. *BMC Biol.* **15**, 53 (2017). doi:10.1186/s12915-017-0392-4 Medline
5. F. Ginhoux, M. Greter, M. Leboeuf, S. Nandi, P. See, S. Gokhan, M. F. Mehler, S. J. Conway, L. G. Ng, E. R. Stanley, I. M. Samokhvalov, M. Merad, Fate mapping analysis reveals that adult microglia derive from primitive macrophages. *Science* **330**, 841–845 (2010). doi:10.1126/science.1194637 Medline
6. K. Kierdorf, D. Erny, T. Goldmann, V. Sander, C. Schulz, E. G. Perdiguero, P. Wieghofer, A. Heinrich, P. Riemke, C. Hölscher, D. N. Müller, B. Luckow, T. Brocker, K. Debowski, G. Fritz, G. Opdenakker, A. Diefenbach, K. Biber, M. Heikenwalder, F. Geissmann, F. Rosenbauer, M. Prinz, Microglia emerge from erythromyeloid precursors via Pu.1- and Irf8-dependent pathways. *Nat. Neurosci.* **16**, 273–280 (2013). doi:10.1038/nn.3318 Medline
7. C. Schulz, E. Gomez Perdiguero, L. Chorro, H. Szabo-Rogers, N. Cagnard, K. Kierdorf, M. Prinz, B. Wu, S. E. W. Jacobsen, J. W. Pollard, J. Frampton, K. J. Liu, F. Geissmann, A lineage of myeloid cells independent of Myb and hematopoietic stem cells. *Science* **336**, 86–90 (2012). doi:10.1126/science.1219179 Medline
8. M. Guilliams, C. L. Scott, Does niche competition determine the origin of tissue-resident macrophages? *Nat. Rev. Immunol.* **17**, 451–460 (2017). doi:10.1038/nri.2017.42 Medline
9. B. Ajami, J. L. Bennett, C. Krieger, W. Tetzlaff, F. M. V. Rossi, Local self-renewal can sustain CNS microglia maintenance and function throughout adult life. *Nat. Neurosci.* **10**, 1538–1543 (2007). doi:10.1038/nn2014 Medline
10. M. R. P. Elmore, A. R. Najafi, M. A. Koike, N. N. Dagher, E. E. Spangenberg, R. A. Rice, M. Kitazawa, B. Matusow, H. Nguyen, B. L. West, K. N. Green, Colony-stimulating factor 1 receptor signaling is necessary for microglia viability, unmasking a microglia progenitor cell in the adult brain. *Neuron* **82**, 380–397 (2014). doi:10.1016/j.neuron.2014.02.040 Medline
11. J. C. Cronk, A. J. Filiano, A. Louveau, I. Marin, R. Marsh, E. Ji, D. H. Goldman, I. Smirnov, N. Geraci, S. Acton, C. C. Overall, J. Kipnis, Peripherally derived macrophages can engraft the brain independent of irradiation and maintain an identity distinct from microglia. *J. Exp. Med.* **215**, 1627–1647 (2018). doi:10.1084/jem.20180247 Medline
12. F. C. Bennett, M. L. Bennett, F. Yaqoob, S. B. Mulinyawe, G. A. Grant, M. Hayden Gephart, E. D. Plowey, B. A. Barres, A combination of ontogeny and CNS environment establishes microglial identity. *Neuron* **98**, 1170–1183.e8 (2018). doi:10.1016/j.neuron.2018.05.014 Medline
13. J. Herz, A. J. Filiano, A. Smith, N. Yogev, J. Kipnis, Myeloid cells in the central nervous system. *Immunity* **46**, 943–956 (2017). doi:10.1016/j.immuni.2017.06.007 Medline
14. M. J. C. Jordão, R. Sankowski, S. M. Brendecke, G. Sagar, G. Locatelli, Y. H. Tai, T. L. Tay, E. Schramm, S. Armbruster, N. Hagemeyer, O. Groß, D. Mai, Ö. Çiçek, T. Falk, M. Kerschensteiner, D. Grün, M. Prinz, Single-cell profiling identifies myeloid cell subsets with distinct fates during neuroinflammation. *Science* **363**, eaat7554 (2019). doi:10.1126/science.aat7554 Medline
15. S. Mundt, D. Mrdjen, S. G. Utz, M. Greter, B. Schreiner, B. Becher, Conventional DCs sample and present myelin antigens in the healthy CNS and allow parenchymal T cell entry to initiate neuroinflammation. *Sci. Immunol.* **4**, eaau8380 (2019). doi:10.1126/sciimmunol.aau8380 Medline
16. D. Mrdjen, A. Pavlovic, F. J. Hartmann, B. Schreiner, S. G. Utz, B. P. Leung, I. Lelios, F. L. Heppner, J. Kipnis, D. Merkler, M. Greter, B. Becher, High-dimensional single-cell mapping of central nervous system immune cells reveals distinct myeloid subsets in health, aging, and disease. *Immunity* **48**, 380–395.e6 (2018). doi:10.1016/j.immuni.2018.01.011 Medline
17. S. G. Utz, P. See, W. Mildenberger, M. S. Thion, A. Silvin, M. Lutz, F. Ingelfinger, N. A. Rayan, I. Lelios, A. Buttgereit, K. Asano, S. Prabhakar, S. Garel, B. Becher, F. Ginhoux, M. Greter, Early fate defines microglia and non-parenchymal brain macrophage development. *Cell* **181**, 557–573.e18 (2020). doi:10.1016/j.cell.2020.03.021 Medline
18. H. Van Hove, L. Martens, I. Scheyltjens, K. De Vlaminck, A. R. Pombo Antunes, S. De Prijck, N. Vandamme, S. De Schepper, G. Van Isterdael, C. L. Scott, J. Aerts, G. Berx, G. E. Boeckxstaens, R. E. Vandenbroucke, L. Vereecke, D. Moechars, M. Guilliams, J. A. Van Ginderachter, Y. Saeys, K. Movahedi, A single-cell atlas of mouse brain macrophages reveals unique transcriptional identities shaped by ontogeny and tissue environment. *Nat. Neurosci.* **22**, 1021–1035 (2019). doi:10.1038/s41593-019-0393-4 Medline
19. B. Korin, T. L. Ben-Shaanan, M. Schiller, T. Dubovik, H. Azulay-Debby, N. T. Boshnak, T. Koren, A. Rolls, High-dimensional, single-cell characterization of the brain's immune compartment. *Nat. Neurosci.* **20**, 1300–1309 (2017). doi:10.1038/nn.4610 Medline
20. B. Ajami, N. Samusik, P. Wieghofer, P. P. Ho, A. Crotti, Z. Bjornson, M. Prinz, W. J. Fantl, G. P. Nolan, L. Steinman, Single-cell mass cytometry reveals distinct populations of brain myeloid cells in mouse neuroinflammation and neurodegeneration models. *Nat. Neurosci.* **21**, 541–551 (2018). doi:10.1038/s41593-018-0100-x Medline
21. F. Herisson, V. Frodermann, G. Courties, D. Rohde, Y. Sun, K. Vandoorne, G. R. Wojtkiewicz, G. S. Masson, C. Vinegoni, J. Kim, D.-E. Kim, R. Weissleder, F. K. Swirski, M. A. Moskowitz, M. Nahrendorf, Direct vascular channels connect skull bone marrow and the brain surface enabling myeloid cell migration. *Nat. Neurosci.* **21**, 1209–1217 (2018). doi:10.1038/s41593-018-0213-2 Medline
22. H. Yao, T. T. Price, G. Cantelli, B. Ngo, M. J. Warner, L. Olivere, S. M. Ridge, E. M. Jablonski, J. Therrien, S. Tannheimer, C. M. McCall, A. Chenn, D. A. Sipkins, Leukaemia hijacks a neural mechanism to invade the central nervous system. *Nature* **560**, 55–60 (2018). doi:10.1038/s41586-018-0342-5 Medline
23. R. Cai, C. Pan, A. Ghasemigharagoz, M. I. Todorov, B. Förstera, S. Zhao, H. S. Bhatia, A. Parra-Damas, L. Mrowka, D. Theodorou, M. Rempfler, A. L. R. Xavier, B. T. Kress, C. Benakis, H. Steinke, S. Liebscher, I. Bechmann, A. Liesz, B. Menze, M. Kerschensteiner, M. Nedergaard, A. Ertürk, Panoptic imaging of transparent mice reveals whole-body neuronal projections and skull-meninges connections. *Nat. Neurosci.* **22**, 317–327 (2019). doi:10.1038/s41593-018-0301-3 Medline
24. J. Rustenhoven, A. Drieu, T. Mamuladze, K. A. de Lima, T. Dykstra, M. Wall, Z. Papadopoulos, M. Kanamori, A. F. Salvador, W. Baker, M. Lemieux, S. Da Mesquita, A. Cugurra, J. Fitzpatrick, S. Sviben, R. Kossina, P. Bayguinov, R. R. Townsend, Q. Zhang, P. Erdmann-Gilmore, I. Smirnov, M.-B. Lopes, J. Herz, J. Kipnis, Functional characterization of the dural sinuses as a neuroimmune interface. *Cell* **184**, 1000–1016.e27 (2021). doi:10.1016/j.cell.2020.12.040 Medline
25. S. Brioschi, W.-L. Wang, V. Peng, M. Wang, I. Shchukina, Z. J. Greenberg, J. K. Bando, N. Jaeger, R. S. Czepielewski, A. Swain, D. A. Mogilenko, W. L. Beatty, P. Bayguinov, J. A. J. Fitzpatrick, L. G. Schuettpelz, C. C. Fronick, I. Smirnov, J. Kipnis, V. S. Shapiro, G. F. Wu, S. Gilfillan, M. Cella, M. N. Artyomov, S. H. Kleinstein, M. Colonna, Heterogeneity of meningeal B cells reveals a lymphopoietic niche at the CNS borders. *Science* 10.1126/science.abf9277 (2021).
26. S. Nowotschin, A.-K. Hadjantonakis, Use of KikGR a photoconvertible green-to-red fluorescent protein for cell labeling and lineage analysis in ES cells and mouse embryos. *BMC Dev. Biol.* **9**, 49 (2009). doi:10.1186/1471-213X-9-49 Medline
27. M. V. Russo, L. L. Latour, D. B. McGavern, Distinct myeloid cell subsets promote meningeal remodeling and vascular repair after mild traumatic brain injury. *Nat. Immunol.* **19**, 442–452 (2018). doi:10.1038/s41590-018-0086-2 Medline
28. M. Yu, L. Ma, Y. Yuan, X. Ye, A. Montagne, J. He, T.-V. Ho, Y. Wu, Z. Zhao, N. Sta Maria, R. Jacobs, M. Urata, H. Wang, B. V. Zlokovic, J.-F. Chen, Y. Chai, Cranial suture regeneration mitigates skull and neurocognitive defects in

craniosynostosis. *Cell* **184**, 243–256.e18 (2021). doi:10.1016/j.cell.2020.11.037 Medline
29. G. J. Randolph, Emigration of monocyte-derived cells to lymph nodes during resolution of inflammation and its failure in atherosclerosis. *Curr. Opin. Lipidol.* **19**, 462–468 (2008). doi:10.1097/MOL.0b013e32830d5f09 Medline
30. P. Mastorakos, D. McGavern, The anatomy and immunology of vasculature in the central nervous system. *Sci. Immunol.* **4**, eaav0492 (2019). doi:10.1126/sciimmunol.aav0492 Medline
31. A. Giladi, L. K. Wagner, H. Li, D. Dörr, C. Medaglia, F. Paul, A. Shemer, S. Jung, S. Yona, M. Mack, A. Leutz, I. Amit, A. Mildner, Cxcl10^{+} monocytes define a pathogenic subset in the central nervous system during autoimmune neuroinflammation. *Nat. Immunol.* **21**, 525–534 (2020). doi:10.1038/s41590-020-0661-1 Medline
32. C. A. Wagner, P. J. Roqué, J. M. Goverman, Pathogenic T cell cytokines in multiple sclerosis. *J. Exp. Med.* **217**, e20190460 (2020). doi:10.1084/jem.20190460 Medline
33. R. Shechter, O. Miller, G. Yovel, N. Rosenzweig, A. London, J. Ruckh, K.-W. Kim, E. Klein, V. Kalchenko, P. Bendel, S. A. Lira, S. Jung, M. Schwartz, Recruitment of beneficial M2 macrophages to injured spinal cord is orchestrated by remote brain choroid plexus. *Immunity* **38**, 555–569 (2013). doi:10.1016/j.immuni.2013.02.012 Medline
34. S. Bovetti, Y.-C. Hsieh, P. Bovolin, I. Perroteau, T. Kazunori, A. C. Puche, Blood vessels form a scaffold for neuroblast migration in the adult olfactory bulb. *J. Neurosci.* **27**, 5976–5980 (2007). doi:10.1523/JNEUROSCI.0678-07.2007 Medline
35. V. A. Cuddapah, S. Robel, S. Watkins, H. Sontheimer, A neurocentric perspective on glioma invasion. *Nat. Rev. Neurosci.* **15**, 455–465 (2014). doi:10.1038/nrn3765 Medline
36. A. Chauveau, G. Pirgova, H.-W. Cheng, A. De Martin, F. Y. Zhou, S. Wideman, J. Rittscher, B. Ludewig, T. I. Arnon, Visualization of T cell migration in the spleen reveals a network of perivascular pathways that guide entry into T zones. *Immunity* **52**, 794–807.e7 (2020). doi:10.1016/j.immuni.2020.03.010 Medline
37. T. L. Roth, D. Nayak, T. Atanasijevic, A. P. Koretsky, L. L. Latour, D. B. McGavern, Transcranial amelioration of inflammation and cell death after brain injury. *Nature* **505**, 223–228 (2014). doi:10.1038/nature12808 Medline
38. C. Baccin, J. Al-Sabah, L. Velten, P. M. Helbling, F. Grünschläger, P. Hernández-Malmierca, C. Nombela-Arrieta, L. M. Steinmetz, A. Trumpp, S. Haas, Combined single-cell and spatial transcriptomics reveal the molecular, cellular and spatial bone marrow niche organization. *Nat. Cell Biol.* **22**, 38–48 (2020). doi:10.1038/s41556-019-0439-6 Medline
39. A. Louveau, J. Herz, M. N. Alme, A. F. Salvador, M. Q. Dong, K. E. Viar, S. G. Herod, J. Knopp, J. C. Setliff, A. L. Lupi, S. Da Mesquita, E. L. Frost, A. Gaultier, T. H. Harris, R. Cao, S. Hu, J. R. Lukens, I. Smirnov, C. C. Overall, G. Oliver, J. Kipnis, CNS lymphatic drainage and neuroinflammation are regulated by meningeal lymphatic vasculature. *Nat. Neurosci.* **21**, 1380–1391 (2018). doi:10.1038/s41593-018-0227-9 Medline
40. S. Da Mesquita, A. Louveau, A. Vaccari, I. Smirnov, R. C. Cornelison, K. M. Kingsmore, C. Contarino, S. Onengut-Gumuscu, E. Farber, D. Raper, K. E. Viar, R. D. Powell, W. Baker, N. Dabhi, R. Bai, R. Cao, S. Hu, S. S. Rich, J. M. Munson, M. B. Lopes, C. C. Overall, S. T. Acton, J. Kipnis, Functional aspects of meningeal lymphatics in ageing and Alzheimer's disease. *Nature* **560**, 185–191 (2018). doi:10.1038/s41586-018-0368-8 Medline
41. S. Da Mesquita, Z. Papadopoulos, T. Dykstra, L. Brase, F. G. Farias, M. Wall, H. Jiang, C. D. Kodira, K. A. de Lima, J. Herz, A. Louveau, D. H. Goldman, A. F. Salvador, S. Onengut-Gumuscu, E. Farber, N. Dabhi, T. Kennedy, M. G. Milam, W. Baker, I. Smirnov, S. S. Rich, B. A. Benitez, C. M. Karch, R. J. Perrin, M. Farlow, J. P. Chhatwal, D. M. Holtzman, C. Cruchaga, O. Harari, J. Kipnis, Dominantly Inherited Alzheimer Network, Meningeal lymphatics affect microglia responses and anti-Aβ immunotherapy. *Nature* **593**, 255–260 (2021). doi:10.1038/s41586-021-03489-0 Medline

ACKNOWLEDGMENTS

We thank S. Smith for editing the manuscript and Anita Impagliazzo for the graphical summary. We thank all the members of the Kipnis laboratory for their valuable comments during numerous discussions of this work. A.C. would like to dedicate this work to the memory of his father, Giorgio Cugurra. **Funding:** This work was conducted with funding from the National Institutes of Health grant AT010416 (J.K.), National Institutes of Health grant AG034113 (J.K.), and National Institutes of Health grant AG057496 (J.K.). **Author contributions:** Initial conceptualization: A.C.; Intellectual contributions; A.C., T.M., J.R., G.B., Z.P., A.D., M.K., J.H., J.K.; Methodology: A.C., T.M., J.R., G.B., Z.G., Z.P., A.D., M.K., S.B., L.S., J.H., M.C., I.S., J.K.; Formal analysis: A.C., T.M., J.R., G.B., T.D., A.D., Z.P.; Investigation: A.C., T.M., J.R., G.B., Z.G., W.B., Z.P., A.D., M.K., S.B., J.H., I.S.; Resources: S.B., L.S., M.C., J.K.; Data Curation: T.D.; Writing: A.C., T.M., J.R., J.K.; Reviewing and Editing: A.C., T.M., J.R., J.K.; Visualization: A.C., T.M., J.R., T.D.; Supervision: J.K; Funding Acquisition: J.K. **Competing interests:** J.K. is a member of a scientific advisory group for PureTech Health. **Data and materials availability:** Single-cell RNA sequencing data are available from Gene Expression Omnibus under accession number GSE161034. All data are available in the main text or the supplementary materials.

SUPPLEMENTARY MATERIALS

science.sciencemag.org/cgi/content/full/science.abf7844/DC1
Figs. S1 to S9
Tables S1 to S5
MDAR Reproducibility Checklist
Movies S1 to S3

24 November 2020; resubmitted 16 April 2021
Accepted 24 May 2021
Published online 3 June 2021
10.1126/science.abf7844

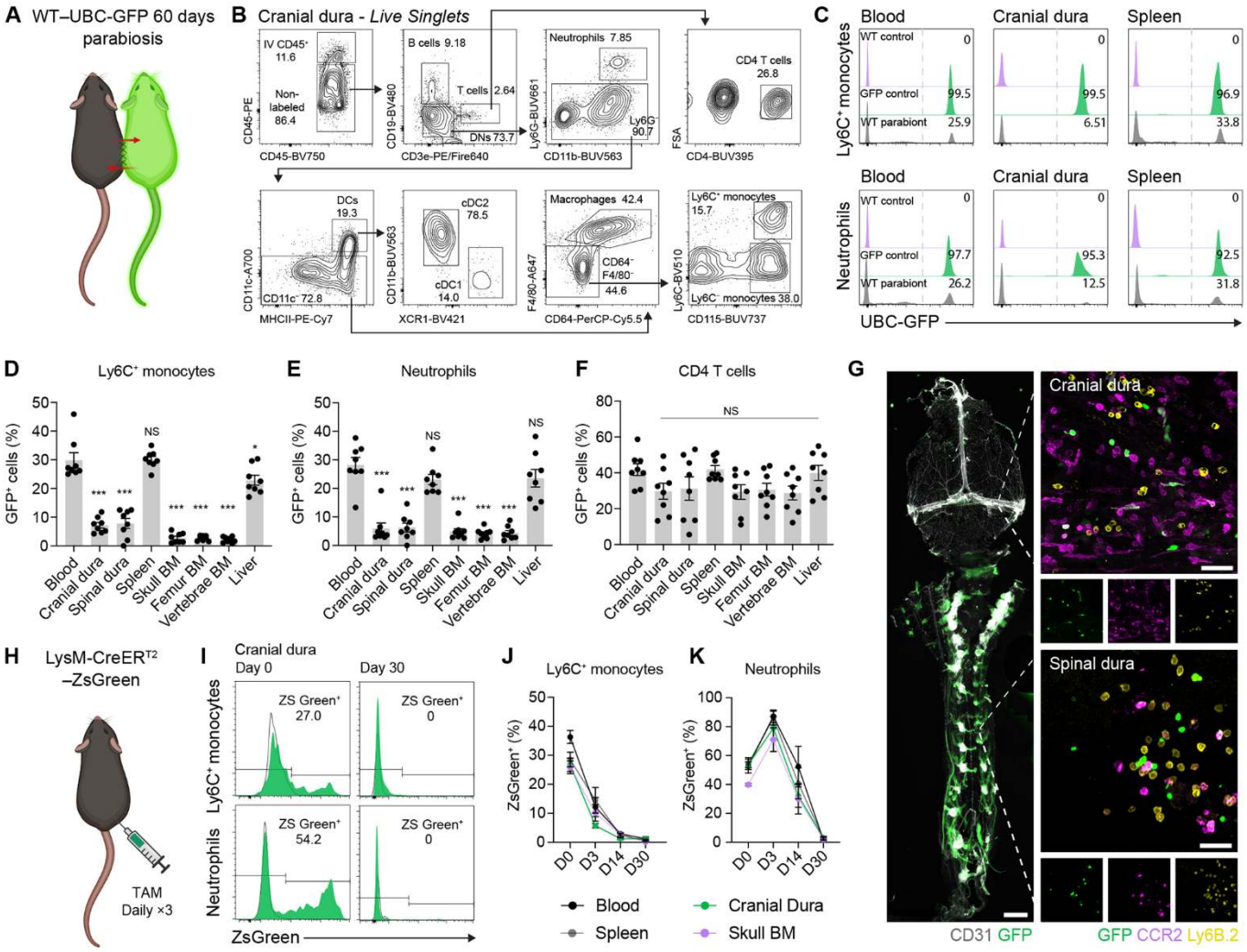

Fig. 1. CNS borders host a substantial pool of monocytes and neutrophils that is not blood-derived. (**A**) Experimental design for parabiosis experiments. WT mice were parabiotically joined with UBC-GFP mice and analyzed 60 days later. (**B**) Representative gating strategy for flow cytometry of immune cells from the cranial dura. (**C**) Representative histograms of GFP$^-$ and GFP$^+$ Ly6C$^+$ monocytes and neutrophils across tissues. WT and UBC-GFP control mice without IV anti-CD45 antibody injection were used to assign gates. (**D** to **F**) Quantification of flow cytometry analysis for GFP$^+$Ly6C$^+$ monocytes, GFP$^+$ neutrophils, and GFP$^+$ CD4 T cells across tissues. NS=not significant, ***P<0.001 versus blood (One-way ANOVA with Dunnett's post hoc test), n=8 mice per tissue, representative of three independent experiments. Data are means ± SEM. (**G**) Representative images from three mice of cranial and spinal dura whole mounts from WT parabionts 60 days after parabiotic pairing. Scale bars, (left) 2000 µm; (right) 50 µm. (**H** to **K**) Myeloid fate mapping strategy using LysM-CreERT2::ZsGreen reporter mice to assess the half-life of meningeal Ly6C$^+$ monocytes and GFP$^+$ neutrophils. Mice received daily tamoxifen injections for 3 days and were then analyzed at four different time points. Cre$^-$ animals were used as controls to assign gates. Black outlined histograms represent Cre$^-$ controls and green histograms represent LysM-CreERT2::ZsGreen reporter mice. n=3-4 mice per group, representative of two independent experiments. Data are means ± SEM.

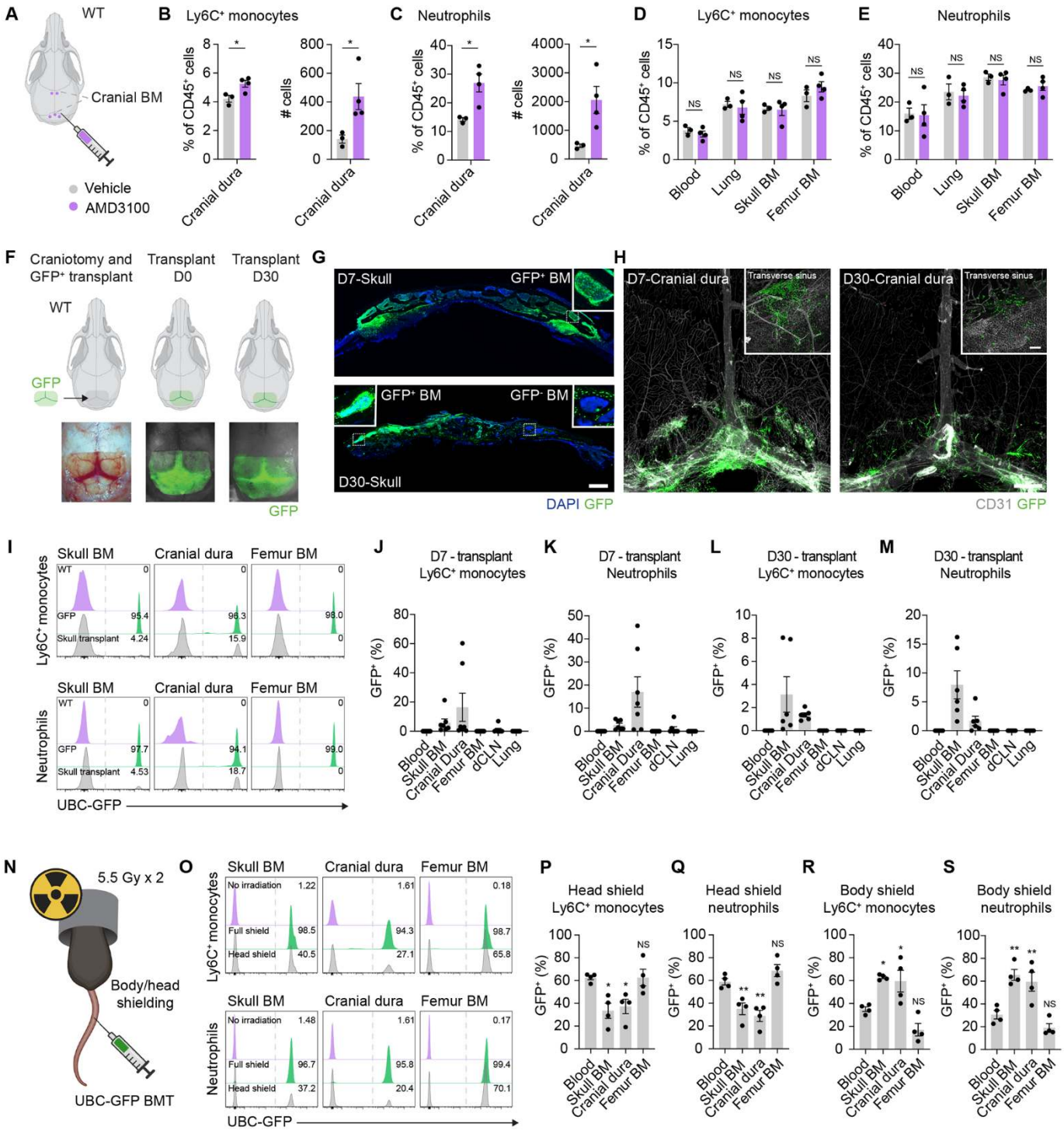
A
WT
Cranial BM
Vehicle
AMD3100
B
Ly6C⁺ monocytes
% of CD45⁺ cells
# cells
Cranial dura
C
Neutrophils
D
Ly6C⁺ monocytes
E
Neutrophils
Blood
Lung
Skull BM
Femur BM
NS
F
Craniotomy and GFP⁺ transplant
Transplant D0
Transplant D30
WT
GFP
G
D7-Skull
GFP⁺ BM
GFP⁻ BM
D30-Skull
DAPI GFP
H
D7-Cranial dura
Transverse sinus
D30-Cranial dura
CD31 GFP
I
Skull BM
Cranial dura
Femur BM
Ly6C⁺ monocytes
Neutrophils
Skull transplant
UBC-GFP
J
D7 - transplant
Ly6C⁺ monocytes
GFP⁺ (%)
K
D7 - transplant
Neutrophils
L
D30 - transplant
Ly6C⁺ monocytes
M
D30 - transplant
Neutrophils
dCLN
N
5.5 Gy x 2
Body/head shielding
UBC-GFP BMT
O
No irradiation
Full shield
Head shield
P
Head shield
Ly6C⁺ monocytes
Q
Head shield
neutrophils
R
Body shield
Ly6C⁺ monocytes
S
Body shield
neutrophils

Fig. 2. Skull bone marrow supplies brain borders with myeloid cells. (**A**) Experimental design for bone marrow egress experiments. Outer periosteal layer of the skull bone was thinned near the bone marrow sites and 1 µl of CXCR4 antagonist AMD3100 (1 µg/ml) or a vehicle was applied to five sites for 5 min. (**B** and **C**) Quantification for flow cytometry analysis of IV-CD45$^-$Ly6C$^+$ monocytes and neutrophils in cranial dura 1 day after AMD3100 administration. **P*<0.05 (Student's *t* test), n=3-4 mice per group, representative of two independent experiments. Data are means ± SEM. (**D** and **E**) Quantification for flow cytometry analysis of IV-CD45$^-$Ly6C$^+$ monocytes and neutrophils in control tissues 1 day after AMD3100 administration. NS=not significant (Two-way ANOVA with Sidak's post hoc test), n=3-4 mice per group, representative of two independent experiments. Data are means ± SEM. (**F**) Schematic representation of the calvaria flap transplantation experiments. Images were taken on anesthetized mice by stereomicroscopy immediately after craniotomy (left), after the subsequent calvaria flap transplantation (middle) and 30 days after the transplantation (right). (**G**) Representative images from three mice of GFP$^+$ calvaria flaps 7 and 30 days after the transplantation. Inserts show GFP$^+$ bone marrow 7 and 30 days after the transplantation. Dead bone marrow was replaced by non-GFP$^+$ cells. Scale bar, 500 µm. (**H**) Representative images from four mice of cranial dura 7 and 30 days after the transplantation showing GFP$^+$ cells below the transfer site. Scale bar, 1000 µm. (**I**) Representative histograms of GFP$^-$ and GFP$^+$ Ly6C$^+$ monocytes and neutrophils across tissues. WT and UBC-GFP control mice without IV anti-CD45 antibody injection were used to assign gates. (**J** to **M**) Quantification of flow cytometry analysis of IV-CD45$^-$GFP$^+$Ly6C$^+$ monocytes and GFP$^+$ neutrophils from calvaria flap transplanted mice, n=6-7 mice per group, representative of 2 independent experiments for day 7 and 3 independent experiments for day 30. Data are means ± SEM. (**N**) Experimental design of irradiation and bone marrow transplantation experiments with different shielding strategies. Four million GFP$^+$ bone marrow cells were intravenously transplanted into head-shielded or body-shielded WT mice after split-dose 11 Gy irradiation. (**O**) Representative histograms of GFP$^-$ and GFP$^+$ Ly6C$^+$ monocytes and neutrophils across tissues. Fully irradiated and non-irradiated mice transplanted with UBC-GFP cells without IV anti-CD45 antibody injection were used as control animals and to assign gates. (**P** to **S**) Quantification of flow cytometry analysis for IV-CD45$^-$ GFP$^+$Ly6C$^+$ monocytes and GFP$^+$ neutrophils in BMT experiments. NS=not significant, **P*<0.05, ***P*<0.01 versus blood (one-way ANOVA with Dunnett's post hoc test), n=4 mice per tissue, representative of two independent experiments. Data are means ± SEM. BM, bone marrow.

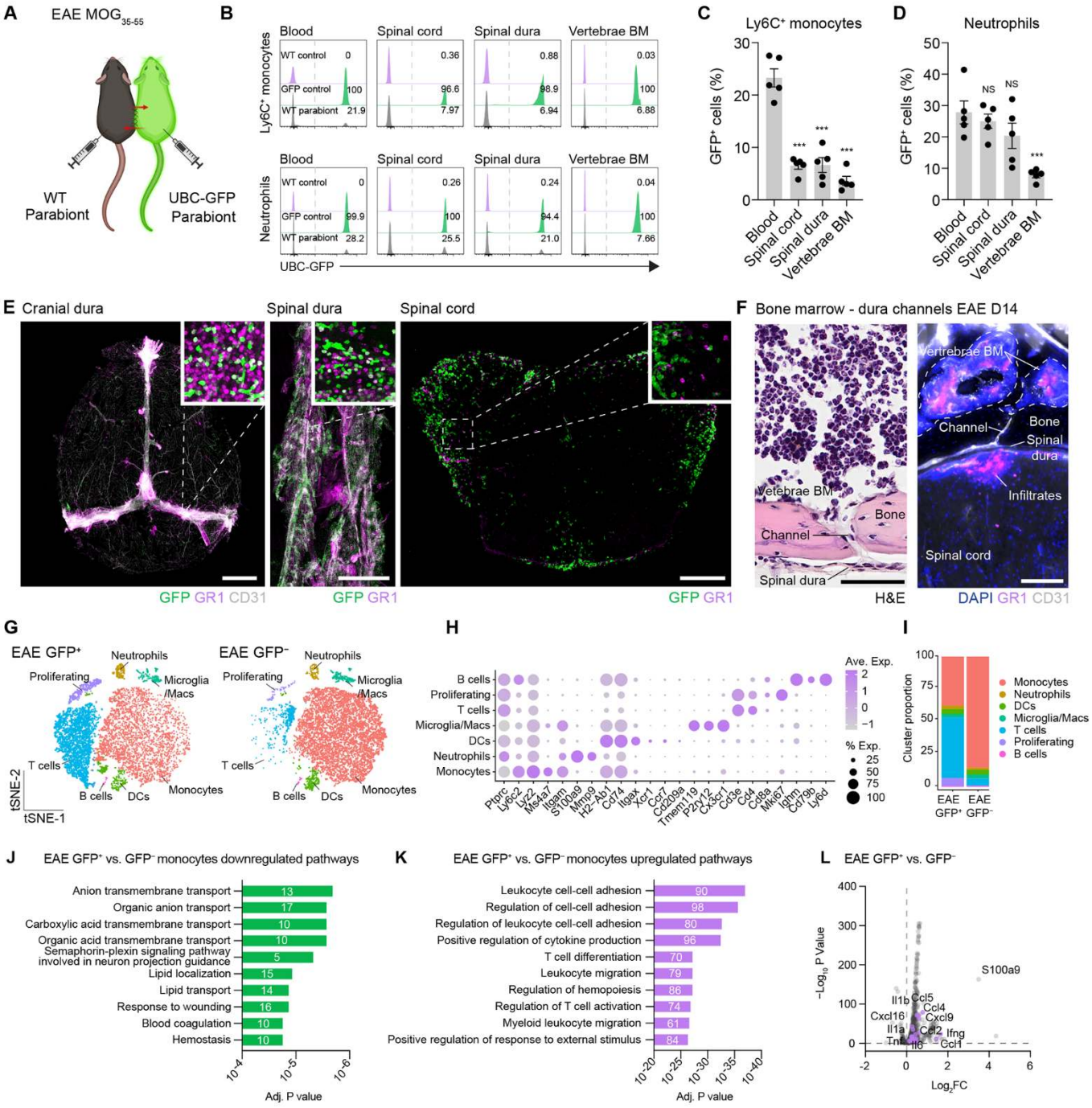
A
EAE MOG35-55
WT Parabiont
UBC-GFP Parabiont
B
Blood
Spinal cord
Spinal dura
Vertebrae BM
Ly6C+ monocytes
WT control
GFP control
WT parabiont
Neutrophils
UBC-GFP
C
Ly6C+ monocytes
GFP+ cells (%)
D
Neutrophils
NS
E
Cranial dura
Spinal dura
Spinal cord
GFP GR1 CD31
GFP GR1
F
Bone marrow - dura channels EAE D14
Vertebrae BM
Channel
Bone
Spinal dura
Infiltrates
Spinal cord
H&E
DAPI GR1 CD31
G
EAE GFP+
EAE GFP−
Neutrophils
Proliferating
Microglia /Macs
T cells
B cells
DCs
Monocytes
tSNE-1
tSNE-2
H
Ave. Exp.
% Exp.
I
Cluster proportion
Monocytes
Neutrophils
DCs
Microglia/Macs
T cells
Proliferating
B cells
J
EAE GFP+ vs. GFP− monocytes downregulated pathways
Anion transmembrane transport
Organic anion transport
Carboxylic acid transmembrane transport
Organic acid transmembrane transport
Semaphorin-plexin signaling pathway involved in neuron projection guidance
Lipid localization
Lipid transport
Response to wounding
Blood coagulation
Hemostasis
Adj. P value
K
EAE GFP+ vs. GFP− monocytes upregulated pathways
Leukocyte cell-cell adhesion
Regulation of cell-cell adhesion
Regulation of leukocyte cell-cell adhesion
Positive regulation of cytokine production
T cell differentiation
Leukocyte migration
Regulation of hemopoiesis
Regulation of T cell activation
Myeloid leukocyte migration
Positive regulation of response to external stimulus
Adj. P value
L
EAE GFP+ vs. GFP−
−Log10 P Value
Log2FC
S100a9

Fig. 3. The inflamed CNS is infiltrated by blood and CNS-adjacent bone marrow-derived myeloid cells. (**A**) Experimental design for EAE induction in parabiotic mice. Sixty days after WT and UBC-GFP mice were paired, EAE was induced in both mice by MOG_{35-55} immunization and the WT mice were analyzed 15 days post-induction. (**B**) Representative histograms of GFP^- and GFP^+ $Ly6C^+$ monocytes and neutrophils across tissues. WT and UBC-GFP control mice without IV anti-CD45 antibody injections were used to assign gates. (**C** and **D**) Quantification of flow cytometry analysis of IV-$CD45^-GFP^+Ly6C^+$ monocytes and GFP^+ neutrophils in EAE-induced WT parabionts. NS=not significant, ***P<0.001 versus blood (one-way ANOVA with Dunnett's post hoc test), n=5 mice per tissue, representative of two independent experiments. Data are means ± SEM. (**E**) Representative images from three mice of cranial dura, spinal dura, and spinal cord sections of WT parabionts 15 days after the EAE induction. Only a minor portion of GFP^+ cells are co-stained with GR1. Scale bars, (left) 2000 μm; (middle) 2000 μm; (right) 200 μm. (**F**) Representative H&E and immunohistochemistry images from five mice of vascular channels found in vertebrae connecting bone marrow to underlying spinal dura. On the left, cells can be seen within channels connecting bone marrow and spinal dura. On the right, $GR1^+$ infiltrates are closely associated with the $CD31^+$ vascular channel. Scale bars, (left) 100 μm; (right) 100 μm. (**G**) tSNE visualizations of color-coded scRNA-seq analysis based on cell types for $CD45^{hi}$IV-$CD45^-GFP^-$ or GFP^+ populations from the spinal cord of WT parabionts 15 days post EAE induction. n=3 pooled mice per sample. (**H**) Dot plots demonstrating scaled gene expression and percentage of cells expressing these genes for cluster phenotyping markers. (**I**) Cluster distributions detailing proportions of cell types in IV-$CD45^-CD45^{hi}GFP^-$ and GFP^+ samples from scRNA-seq analysis. (**J** and **K**) Top 10 down-regulated and up-regulated GO Biological Process terms describing differentially expressed genes between GFP^+ and GFP^- monocytes from scRNA-seq analysis. Numbers in bar graphs represent the number of differentially expressed genes belonging to that pathway. (**L**) Volcano plot showing differentially expressed genes between GFP^+ and GFP^- monocytes from scRNA-seq analysis. Inflammatory chemokines, and cytokines are highlighted.